scientific reports

Check for updates

OPEN

Event topology and global observables in heavy-ion collisions at the Large Hadron Collider

Suraj Prasad[1], Neelkamal Mallick[1], Debadatta Behera[1], Raghunath Sahoo[1,2]✉ & Sushanta Tripathy[3]

Particle production and event topology are very strongly correlated in high-energy hadronic and nuclear collisions. Event topology is decided by the underlying particle production dynamics and medium effects. Transverse spherocity is an event shape observable, which has been used in pp and heavy-ion collisions to separate the events based on their geometrical shapes. It has the unique capability to distinguish between jetty and isotropic events. In this work, we have implemented transverse spherocity in Pb–Pb collisions at $\sqrt{s_{\rm NN}}$ = 5.02 TeV using A Multi-Phase Transport Model (AMPT). While awaiting for experimental explorations, we perform a feasibility study of transverse spherocity dependence of some of the global observables in heavy-ion collisions at the Large Hadron Collider energies. These global observables include the Bjorken energy density ($\varepsilon_{\rm Bj}$), squared speed of sound (c_s^2) in the medium and the kinetic freeze-out properties for different collision centralities. The present study reveals about the usefulness of event topology dependent measurements in heavy-ion collisions.

Heavy-ion collisions at the ultra-relativistic energies aim to produce a deconfined state of quarks and gluons, the primordial matter believed to have formed at the infancy of the Universe. The matter created in such collisions at the Relativistic Heavy-Ion Collider (RHIC) at the Brookhaven National Laboratory, USA and at the Large Hadron Collider (LHC) at European Center for Nuclear Research (CERN), Switzerland gives an opportunity to study its properties at the extreme conditions of temperature and energy densities. Global properties of the created matter such as total charged particle multiplicity in the final state, initial energy density, and temperature of the system play a pivotal role to understand the form of the created matter, while addressing many fundamental questions in basic science. The expansion of the created fireball because of huge concentration of initial energy density and high temperature is probed through the equation of state and hence the speed of sound in the medium. The final state particle abundances are governed by the initial state of the matter—if the collision creates a partonic deconfined colored phase of matter or a confined, color neutral hadronic state. The event topology is governed by the underlying particle production mechanism. For example, a back-to-back momentum conserving shower of particles, called jets is an event topology, whose underlying mechanism is governed by hard perturbative Quantum Chromodynamics (pQCD) high transverse momentum processes, whereas an isotropic geometry in the event topology is mostly rich in soft QCD non-perturbative interactions.

In elementary and hadronic collisions at GeV and TeV energies, although event topology dependent studies have got some level of importance, because of a dense medium formation in heavy-ion collisions, these techniques like sphericity, transverse spherocity, R_T etc. are not applied to heavy-ion collisions. Event topology dependent characterisation of the systems produced in heavy-ion collisions through the global properties are not a well explored area. This is a first attempt to explore the sensitiveness of the global observables in heavy-ion collisions, to the event topology and hence the underlying particle production dynamics. In our recent study[1], we found that the anisotropic flow strongly depends on transverse spherocity in heavy-ion collision systems. Thus, it would be interesting to see how the global properties, often studied in heavy-ion collisions, vary as a function of transverse spherocity. It is worth to note that global properties like Bjorken energy density and speed of sound give insights to the initial state of the produced system while the kinetic freezeout parameters provide insights to the evolution of produced particles in the medium. The use of transverse spherocity along with collision centrality also provides an opportunity to study such observables in a multi-differential way. In the present work, we use transverse spherocity as the event shape observable and study the global properties such as Bjorken energy

[1]Department of Physics, Indian Institute of Technology Indore, Simrol, Indore 453552, India. [2]CERN, CH 1211, Geneva 23, Switzerland. [3]INFN - sezione di Bologna, via Irnerio 46, 40126 Bologna, BO, Italy. ✉email: Raghunath.Sahoo@cern.ch

density, speed of sound and kinetic freeze-out parameters for different centrality classes in Pb–Pb collisions at $\sqrt{s_{\rm NN}}$ = 5.02 TeV using A Multi-Phase Transport Model (AMPT).

The paper is organised as follows. We begin with a brief introduction about the usefulness of event topology studies in heavy-ion collisions. In "Event generation and analysis methodology", the event generation methodology in AMPT and the definition of transverse spherocity is given. We report and discuss the results in "Results and discussion". The results are summarised in "Summary and conclusion".

Event generation and analysis methodology

In this section, we begin with a brief introduction on AMPT model. Then, we proceed to define the transverse spherocity as an event shape analysis tool.

A Multi-phase Transport (AMPT) Model. A Multi-Phase Transport Model contains four components namely[2–6,6–10],

- Initialisation of collisions using HIJING model: the cross-section of the produced mini-jets in pp collisions is calculated and then converted to heavy-ion collisions via inbuilt Glauber model
- Parton transport after initialisation: transportation of produced partons is performed via Zhang's parton cascade model
- Hadronisation mechanism: in string melting version, the transported partons are hadronised using spatial coalescence mechanism; in the default AMPT version, fragmentation mechanism using Lund fragmentation parameters are used for hadronising the transported partons
- Hadron transport: the hadrons undergo evolution in relativistic transport mechanism via meson-baryon, meson-meson and baryon–baryon interactions

As, the particle flow and spectra at the mid-$p_{\rm T}$ regions are well explained by quark coalescence mechanism for hadronisation[6,9,10], we have used string melting mode for all of our calculations. We have used the AMPT version 2.26t7 (released: 28/10/2016) in our current work. The AMPT settings in the current work, are the same as reported in Ref.[1,11]. For the input of impact parameter values for different centralities in Pb–Pb collisions, we have used Ref.[12]. One should note here that, high centrality collisions correspond to low impact parameter values and higher final state charged-particle multiplicity ($\langle dN_{\rm ch}/d\eta\rangle$). Although the concept of centrality is widely used in heavy-ion collisions, in view of a final state multiplicity scaling across collisions species, that is observed at the LHC energies, we may use centrality and $\langle dN_{\rm ch}/d\eta\rangle$ variably in this work.

Transverse spherocity. Transverse spherocity is defined for a unit vector $\hat{n}(n_T, 0)$ that minimizes the ratio[13,14]:

$$S_0 = \frac{\pi^2}{4}\left(\frac{\Sigma_i\,|\mathbf{p}_{T_i}\times\hat{n}|}{\Sigma_i\,p_{T_i}}\right)^2. \tag{1}$$

$\hat{n}$ is an arbitrary unit vector in the transverse plane. To find such a unit vector, one has to perform iteration through all possible values of $\hat{n}$ with azimuthal angle 0 to 2π and select the $\hat{n}$ such that the term inside the bracket given in Eq. (1) becomes minimum for a given event. Here, the index i runs over all the final state hadrons in an event. By construction, transverse spherocity is infrared and collinear safe[15] and the extreme limits are related to specific configurations of events in transverse plane. Transverse spherocity becoming 0 are the events with pencil-like (back-to-back) structure and called as jetty events while 1 would mean the events are isotropic. A schematic picture illustrating the event topology is shown in Fig. 1. For the sake of simplicity, here onwards, the transverse spherocity is referred as spherocity. The spherocity distributions are selected in the pseudorapidity range of $|\eta| < 0.8$ with a minimum constraint of 5 charged particles with $p_{\rm T} > 0.15$ GeV/c to recreate the similar conditions as in ALICE experiment at the LHC. The jetty events are those events having spherocity values in the lowest 20 percent and the isotropic events are those occupying the highest 20 percent in the spherocity distribution of all the events. The spherocity cuts for each centrality are mentioned in Table 1.

Top panel of Fig. 2 shows the spherocity distributions for different centrality classes in Pb–Pb collisions, $\sqrt{s_{\rm NN}} = 5.02$ TeV at mid-rapidity ($|\eta| < 0.8$) using AMPT model and similarly, the bottom panel is the spherocity distribution for different charged particle multiplicity classes in pp collisions, $\sqrt{s} = 13$ TeV at mid-rapidity ($|\eta| < 0.8$) using PYTHIA8[16]. The details of event generation methodology using PYTHIA8 can be found in Ref.[17]. For pp collisions, the charged particle multiplicities are chosen in the acceptance of V0 detector in ALICE at the LHC with pseudorapidity coverage of V0A ($2.8 < \eta < 5.1$) and V0C ($-3.7 < \eta < -1.7$). One should note here that the particle production mechanisms in AMPT and PYTHIA8 models are completely different but we have chosen the tunes of the models where the models describe many of the experimental observables. At a first glance, the spherocity distributions in Pb–Pb collisions look shifted more towards the isotropic limit when compared to the pp collisions, where the distributions are shifted towards the jetty limit. This behavior is understood based on the fact that the system size in Pb–Pb collisions are significantly higher when compared with pp collisions and the medium effect in terms of rescattering helps taking the system towards isotropisation. In comparison to pp collisions, where we observe a distribution of spherocity or in other words, there is an equal production probability of both jetty and isotropic events, medium effects in heavy-ion collisions in principle destroy the jettiness event topology, which is seen from Fig. 2. A skewed distribution of spherocity towards isotropic limit is an indication of the formation of a QCD medium in heavy-ion collisions. When studied as a function of centrality (multiplicity) classes for Pb–Pb (pp) collisions, it is observed that the spherocity

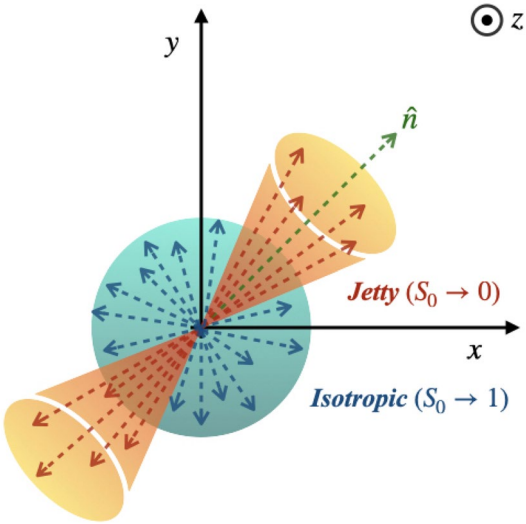

Figure 1. Schematic picture showing jetty and isotropic events in the transverse plane, assuming the z-axis is the beam axis or the longitudinal axis.

Centrality (%)	Low-S_0	High-S_0
0–10	0–0.880	0.953–1
10–20	0–0.813	0.914–1
20–30	0–0.760	0.882–1
30–40	0–0.735	0.869–1
40–50	0–0.716	0.865–1
50–60	0–0.710	0.870–1
60–70	0–0.707	0.873–1
70–100	0–0.535	0.822–1

Table 1. Low 20 % and high 20% cuts on spherocity distribution in Pb–Pb collisions at $\sqrt{s_{\rm NN}} = 5.02$ TeV for different centrality classes.

distributions are shifted towards the isotropic limit for central (high-multiplicity) collisions compared to peripheral (low-multiplicity) collisions.

Now, we proceed to discuss the global properties and their dependence on spherocity classes in the next section. For the sake of simplicity, here onwards we refer $\pi^+ + \pi^-$, $\mathrm{K}^+ + \mathrm{K}^-$, and $\mathrm{p}+\bar{\mathrm{p}}$ as pions, kaons, and protons, respectively.

Results and discussion

Bjorken energy density ($\varepsilon_{\rm Bj}$). In heavy-ion collisions, the transverse energy ($E_{\rm T}$) is one of the significant global observables that is used to study the possible formation of a medium of quarks and gluons under extreme temperature and energy density. Before the collisions, all the energy is carried by the beam particles in longitudinal phase space. But after the collisions, the final state particle production in the transverse plane carries finite transverse energy ($E_{\rm T}$), which is an event-by-event observable and it is closely related to the collision geometry. In the Bjorken boost-invariant hydrodynamics model[18] for relativistic heavy-ion collisions, $E_{\rm T}$ at mid-rapidity gives the quantitative estimation of the initial energy density produced in an interaction. Under boost invariance, the Bjorken energy density ($\varepsilon_{\rm Bj}$) in the nuclear collision zone can be estimated as,

$$\varepsilon_{\rm Bj} = \frac{1}{\tau S_{\rm T}} \frac{dE_{\rm T}}{dy}. \tag{2}$$

where, τ is the formation time and usually taken to be 1 fm/c. $E_{\rm T}$ is the total transverse energy and $S_{\rm T} = \pi R^2$ is the transverse overlap area of the colliding nuclei. As $R = R_0 A^{1/3}$, one replaces $A = N_{part}/2$. That makes the expression for transverse overlap area,

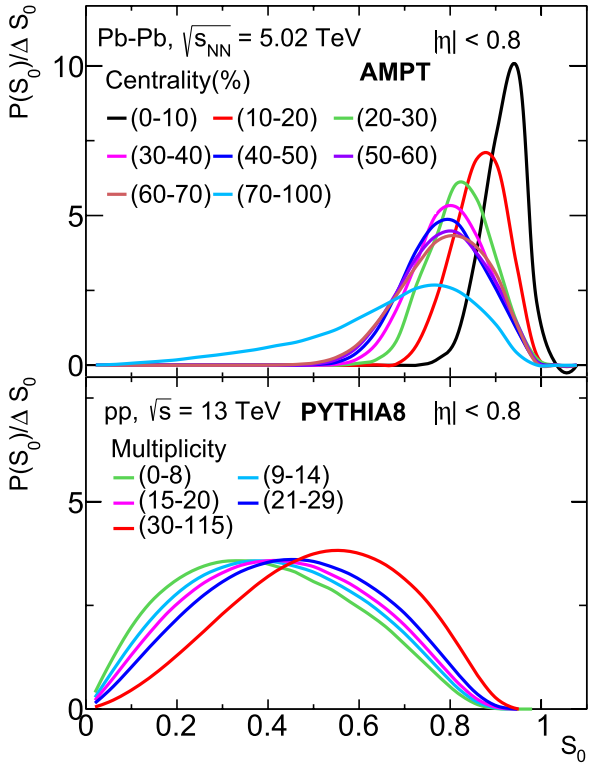

Figure 2. Top (bottom) panel: transverse spherocity distribution for different centrality (multiplicity) classes in Pb–Pb (pp) collisions at $\sqrt{s_{\rm NN}} = 5.02$ TeV ($\sqrt{s} = 13$ TeV) using AMPT (PYTHIA8) model.

$$S_{\rm T} = \pi R_0^2 \left(\frac{N_{part}}{2}\right)^{2/3}. \tag{3}$$

Transverse energy ($E_{\rm T}$) at mid-rapidity region can be approximated as[19–21],

$$\frac{dE_{\rm T}}{dy} \approx \frac{3}{2} \times \left(\langle m_{\rm T}\rangle \frac{dN}{dy}\right)_{\pi^{\pm}} + 2 \times \left(\langle m_{\rm T}\rangle \frac{dN}{dy}\right)_{K^{\pm},p,\bar{p}}. \tag{4}$$

The multiplicative factors 3/2 and 2 account for neutral particles. $m_{\rm T} = \sqrt{p_{\rm T}^2 + m^2}$, is the transverse mass and dN/dy is the integrated yield for $\pi^{\pm}$, $K^{\pm}$ and $p + \bar{p}$ at mid-rapidity region *i.e.* $|y| < 0.5$, estimated for $p_{\rm T} > 0.15$ GeV/c.

Figure 3 shows the mean transverse mass ($\langle m_{\rm T}\rangle$) as a function of different centrality classes in Pb–Pb collisions at $\sqrt{s_{\rm NN}} = 5.02$ TeV at mid-rapidity for $\pi^{\pm}$, $K^{\pm}$ and $p + \bar{p}$ using AMPT model. Except pions, where resonance decay contributions are expected, for all other charged particles $\langle m_{\rm T}\rangle$ shows a decrease towards peripheral collisions. The lower panels of the figure show the effect of event topology on $\langle m_{\rm T}\rangle$, where one observes higher $\langle m_{\rm T}\rangle$ for low-S_0 events (jetty). Figure 4 shows the integrated yield (dN/dy) as a function of different centrality classes in Pb–Pb collisions at $\sqrt{s_{\rm NN}} = 5.02$ TeV at mid-rapidity for different identified particles using AMPT model. As expected, the integrated yield is higher for more central collisions and gradually decreases as we move towards mid-central and peripheral collisions. It can be accounted due to the decrease in the participating partonic matter from central to peripheral collisions. For pions, the integrated yield is higher than kaon and proton, which follows a thermalised Boltzmannian production of particles in a multiparticle production process. The integrated yield as a function of spherocity shows that high-S_0 events have a higher yield than low-S_0 events. It is also clear that the integrated yield is highly dependent on the spherocity classes for most central heavy-ion collisions and the dependence decreases while going towards peripheral collisions.

Figure 5 shows the Bjorken energy density ($\varepsilon_{\rm Bj}$) vs. centrality (%) for high-S_0, S_0-integrated and low-S_0 events in Pb–Pb collisions. We observe a strong dependence of Bjorken energy density on the centrality classes. The values of the initial energy density is observed to be higher than the lattice QCD estimation of 1 GeV/fm^3 energy density for a deconfinement transition[22]. However, we have found that the Bjorken energy density is independent of the spherocity selection and irrespective of the event topology, it is similar for both high-S_0 and low-S_0 events for all collision centralities. It is noteworthy that the Bjorken energy density for a given collision centrality has effects from the number of particles produced and their mean transverse mass. Because of the opposite trends of these two observables with event spherocity, the overall effect cancels out leaving Bjorken energy density to be independent of event topology.

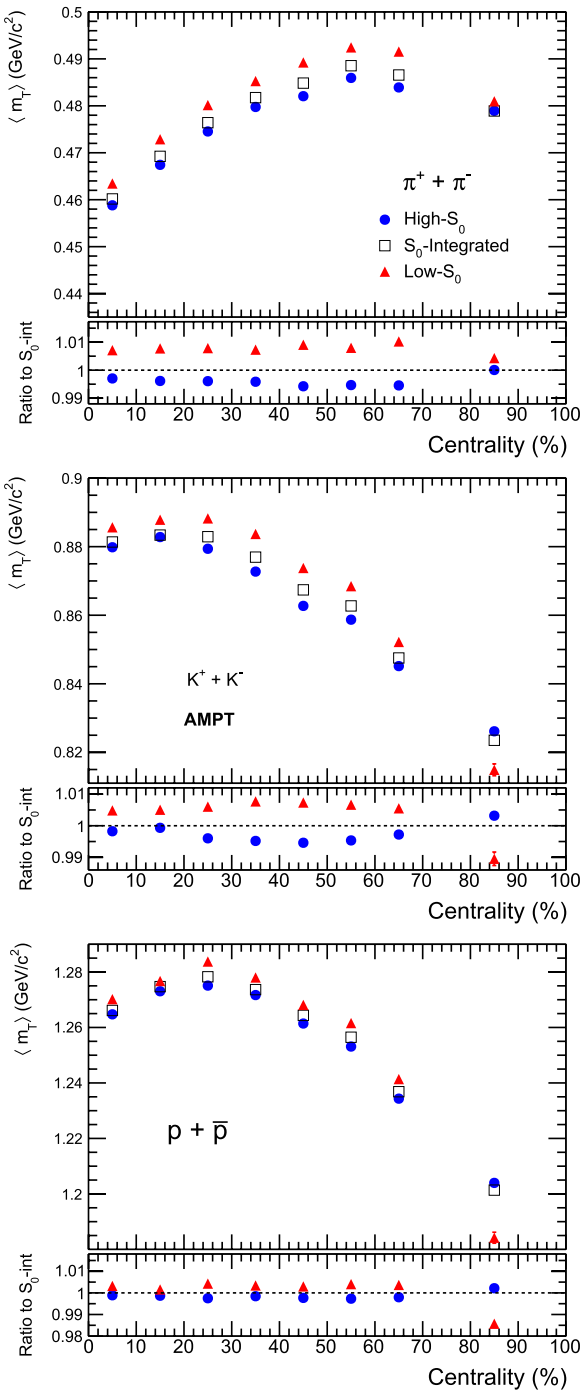

Figure 3. $\langle m_T \rangle$ vs. collision centrality(%) for pions (top), kaons (middle) and protons (bottom) in Pb–Pb collisions with high-S_0, S_0-integrated and low-S_0 events, respectively.

Squared speed of sound (c_s^2) and pseudorapidity distribution. Figure 6 shows pseudorapidity distributions of charged particles in Pb–Pb collisions at $\sqrt{s_{NN}}$ = 5.02 TeV at mid rapidity for (0–10)% and (60–70)% centrality classes in different spherocity classes. Figure 6 complements the observation seen in Fig. 4, where the charged particle multiplicity is found to be higher for high-S_0 events compared to low-S_0 events.

In Landau hydrodynamical model[23], the width of the rapidity distribution is related to the speed of sound (c_s) via the following expression.

$$\sigma_y^2 = \frac{8}{3}\frac{c_s^2}{1-c_s^2} ln\left(\frac{\sqrt{s_{NN}}}{2m_p}\right). \quad (5)$$

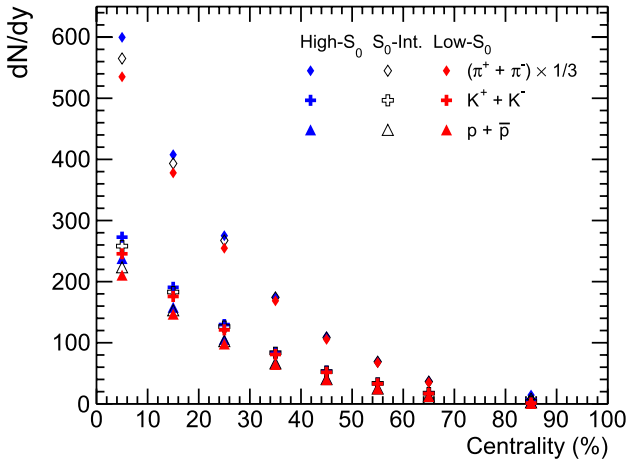

Figure 4. Integrated yield (dN/dy) vs. collision centrality (%) for pions (top), kaons (middle) and protons (bottom) at mid-rapidity in Pb–Pb collisions.

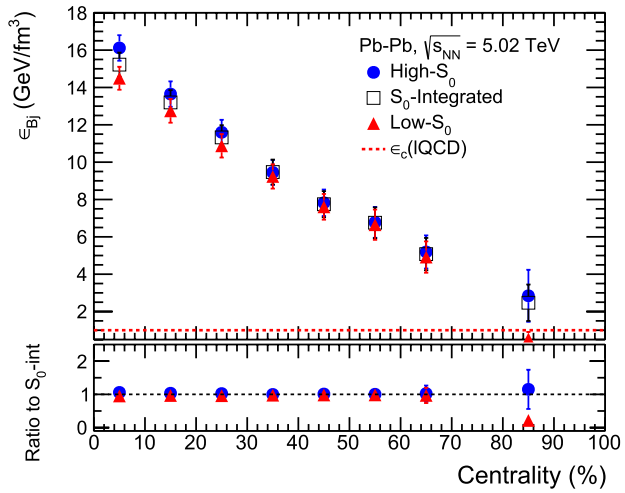

Figure 5. Top plot: Bjorken energy density ($\varepsilon_{\mathrm{Bj}}$) vs. centrality (%) with high-S_0, S_0-integrated and low-S_0 events in Pb–Pb collisions. Bottom plot: ratio of Bjorken energy density ($\varepsilon_{\mathrm{Bj}}$) for high-$S_0$ and low-S_0 events to the S_0-integrated events. The dotted line shows lattice QCD predicted value of critical energy density for a deconfinement transition.

Here, m_p is the mass of proton and σ_y is the width of the rapidity distribution and $c_s^2 = 1/3$ for ideal gas. Due to presence of a dip, it is difficult to fit a single Gaussian function to the pseudorapidity distribution. Generally, in experiments[24] a double Gaussian function is used to fit the pseudorapidity distribution, which is given by,

$$A_1 e^{\frac{-\eta^2}{2\sigma_1^2}} - A_2 e^{\frac{-\eta^2}{2\sigma_2^2}}. \tag{6}$$

Here, A_1 and A_2 are normalisation parameters and σ_1 and σ_2 are the widths of the double Gaussian distribution. After fitting we have obtained the values of σ_1 and σ_2. The values of σ_1 and σ_2 are given in Table 2. The fitting has been performed using χ^2 minimisation method and corresponding χ^2/ndf values for the fittings for each spherocity classes across all centralities are shown in Table 3. Here, σ_1 has been used as the default value and the maximum deviation of σ_1 and σ_2 is used for the uncertainty calculation of c_s^2. Figure 7 shows the squared speed of sound as a function of centrality in Pb–Pb collisions at $\sqrt{s_{\mathrm{NN}}}$ = 5.02 TeV for different spherocity classes. The c_s^2 value as a function of centrality shows that for the central collision system, it is higher and gradually decreases towards peripheral collisions. It indicates that central collisions are denser compared to the peripheral collisions. However, c_s^2 is found to be similar for all spherocity classes within uncertainty.

Kinetic freeze-out properties. The hot and dense medium formed in relativistic heavy-ion collisions cools down as the system expands until the kinetic freeze-out is achieved. At kinetic freeze-out, the transverse momentum spectra of the particles are frozen, which carries information about the phase-space distribution of

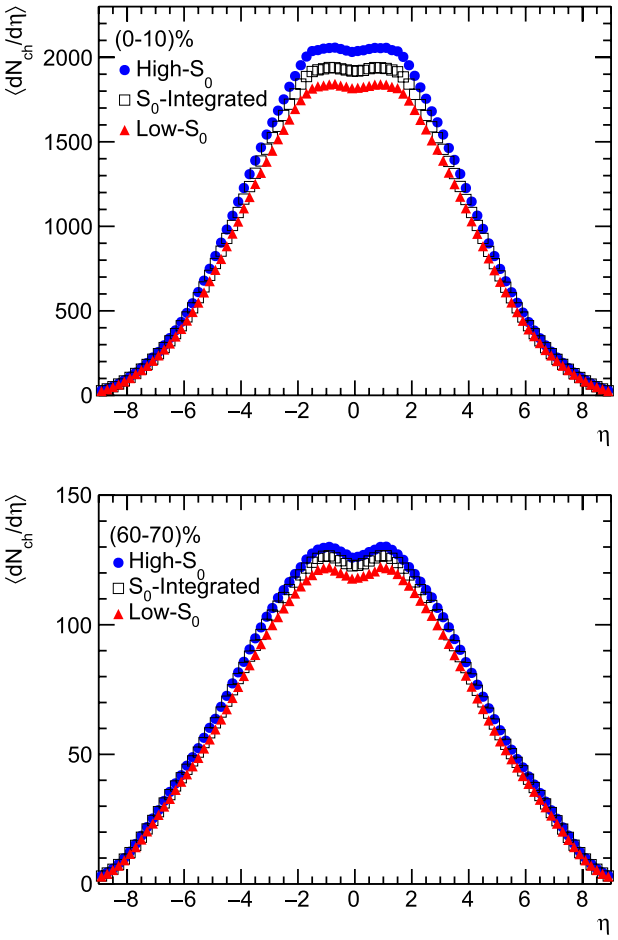

Figure 6. Charged particles pseudorapidity distribution ($dN_{ch}/d\eta$) for high-S_0, S_0-integrated and low-S_0 events for (0–10)% (top) and (60–70)% (bottom) centrality class in Pb–Pb collisions at $\sqrt{s_{\rm NN}}$ = 5.02 TeV.

Centrality(%)	High-S_0		S_0 Integrated		Low-S_0	
	σ_1	σ_2	σ_1	σ_2	σ_1	σ_2
0–10	2.110 ± 0.024	1.757 ± 0.223	2.120 ± 0.023	1.786 ± 0.022	2.079 ± 0.022	1.769 ± 0.020
10–20	2.050 ± 0.019	1.819 ± 0.018	2.053 ± 0.016	1.830 ± 0.016	2.007 ± 0.017	1.797 ± 0.016
20–30	1.946 ± 0.011	1.794 ± 0.019	1.954 ± 0.010	1.807 ± 0.010	1.911 ± 0.010	1.773 ± 0.016
30–40	1.845 ± 0.006	1.751 ± 0.006	1.853 ± 0.006	1.759 ± 0.006	1.830 ± 0.006	1.740 ± 0.006
40–50	1.815 ± 0.004	1.747 ± 0.004	1.803 ± 0.004	1.745 ± 0.004	1.790 ± 0.004	1.731 ± 0.004
50–60	1.755 ± 0.001	1.742 ± 0.001	1.746 ± 0.001	1.733 ± 0.001	1.735 ± 0.003	1.722 ± 0.003
60–70	1.738 ± 0.034	1.731 ± 0.034	1.743 ± 0.003	1.737 ± 0.003	1.729 ± 0.003	1.722 ± 0.003
70–100	1.846 ± 0.001	1.843 ± 0.001	1.799 ± 0.001	1.798 ± 0.001	1.782 ± 0.001	1.781 ± 0.001

Table 2. Double Gaussian width parameters from fitting the pseudorapidity distributions in the range $|\eta| < 2$ using Eq. (6).

the final state of the fireball produced during relativistic heavy-ion collisions. The Boltzmann–Gibbs blastwave (BGBW) distribution[25] can be used to describe the transverse momentum spectra of identified charged particles formed in heavy-ion collisions and one can obtain the transverse radial flow velocity ($\beta_{\rm T}$) and kinetic freeze-out temperature ($T_{\rm kin}$) of the system. The invariant yield in the BGBW framework can be expressed as:

$$E\frac{d^3N}{dp^3} = C\int d^3\sigma_\mu p^\mu exp\left(-\frac{p^\mu u_\mu}{T_{\rm kin}}\right). \tag{7}$$

Here, C is the normalisation constant and p^μ, the particle four momentum is given by,

Centrality(%)	χ^2/ndf		
	High-S_0	S_0 Integrated	Low-S_0
0–10	0.16	0.11	0.13
10–20	0.55	0.45	0.30
20–30	0.92	0.99	1.15
30–40	1.16	1.28	0.97
40–50	1.06	1.17	0.92
50–60	0.64	0.86	0.96
60–70	0.67	0.64	0.91
70–100	0.51	0.35	1.15

Table 3. χ^2 /ndf values for the fitting of $dN_{ch}/d\eta$ to a double Gaussian distribution.

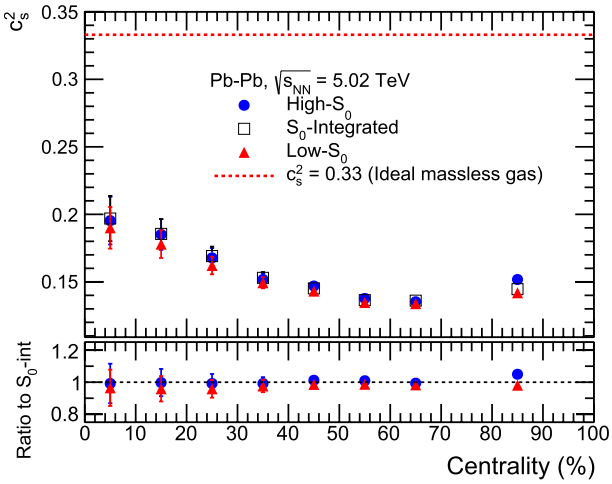

Figure 7. Top plot: Speed of sound (c_s^2) vs. Centrality(%) for high-S_0, S_0-integrated and low-S_0 events in Pb–Pb collisions. Bottom plot: Ratio of speed of sound (c_s^2) for high-S_0 and low-S_0 events to the S_0-integrated events.

$$p^{\mu} = (m_T \cosh y,\ p_T \cos\phi,\ p_T \sin\phi,\ m_T \sinh y). \tag{8}$$

The particle four-velocity is given by,

$$u^{\mu} = \cosh\rho\ (\cosh\eta,\ \tanh\rho\ \cos\phi_r,\ \tanh\rho\ \sin\phi_r,\ \sinh\ \eta), \tag{9}$$

so that

$$p^{\mu}u_{\mu} = m_T \cosh(y-\eta)\cosh\rho - p_T \sinh\rho\cos(\phi-\phi_r). \tag{10}$$

The freeze-out surface is parametrised as,

$$d^3\sigma_{\mu} = (\cosh\eta,\ 0,\ 0,\ -\sinh\eta)\ \tau\ r\ dr\ d\eta\ d\phi_r. \tag{11}$$

Here, η is the space-time rapidity. Now, Eq. (7) can be written as,

$$\left.\frac{d^2N}{dp_T dy}\right|_{y=0} = C\,p_T m_T \int_0^{R_0} r\ dr\ K_1\left(\frac{m_T\ \cosh\rho}{T_{\rm kin}}\right) I_0\left(\frac{p_T\ \sinh\rho}{T_{\rm kin}}\right). \tag{12}$$

Here, $K_1\left(\frac{m_T\ \cosh\rho}{T_{\rm kin}}\right)$ and $I_0\left(\frac{p_T\ \sinh\rho}{T_{\rm kin}}\right)$ are modified Bessel's functions, which are given by,

$$K_1\left(\frac{m_T\ \cosh\rho}{T_{\rm kin}}\right) = \int_0^{\infty} \cosh y\ \exp\left(-\frac{m_T\ \cosh y\ \cosh\rho}{T_{\rm kin}}\right) dy,$$

$$I_0\left(\frac{p_T\ \sinh\rho}{T_{\rm kin}}\right) = \frac{1}{2\pi}\int_0^{2\pi} \exp\left(\frac{p_T\ \sinh\rho\ \cos\phi}{T_{\rm kin}}\right) d\phi,$$

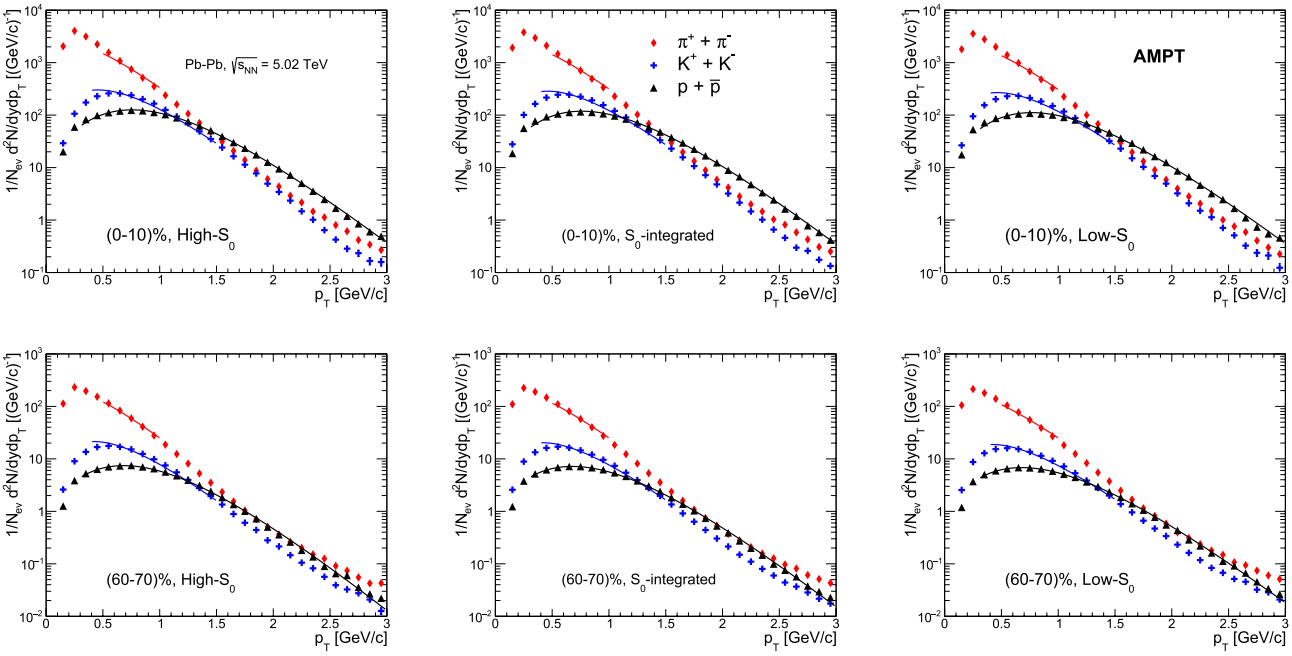

Figure 8. Simultaneous fitting of identified charged particles' p_T spectra with Boltzmann–Gibbs blastwave function for high-S_0 (left), S_0-integrated (middle) and low-S_0 (right) events in Pb–Pb collisions at $\sqrt{s_{NN}}$ = 5.02 TeV. The fitting is shown for (0–10)% (top) and (60-70)% (bottom) centrality classes.

	χ^2/ndf		
Centrality(%)	High-S_0	S_0 Integrated	Low-S_0
0–10	2.7	2.8	3.2
10–20	2.5	2.8	2.8
20–30	2.9	2.8	2.7
30–40	2.8	2.6	2.6
40–50	2.4	2.2	2.1
50–60	2.1	2.1	2.0
60–70	2.4	2.2	1.6
70–100	2.2	2.1	2.4

Table 4. χ^2/ndf values for the simultaneous fitting of identified charged particles' p_T spectra to the BGBW distribution.

where $\rho = \tanh^{-1}\beta_T$ and $\beta_T = \beta_s \xi^n$[25–28]. β_T is called radial flow velocity, $\xi = (r/R_0)$, β_s is the maximum surface velocity, r is the radial distance and R_0 is the maximum radius of the fireball at freeze-out. In this model, the particles closer to the center of the fireball are assumed to move slower than the ones at the edges. The mean transverse velocity is given by[29],

$$\langle \beta_T \rangle = \frac{\int \beta_s \xi^n \xi \, d\xi}{\int \xi \, d\xi} = \left(\frac{2}{2+n}\right)\beta_s. \tag{13}$$

Figure 8 shows the simultaneous BGBW fitting to the identified charged particles' p_T spectra in (0–10)% and (60-70)% centrality classes. The fitting ranges for pions, kaons and protons are (0.5–1) GeV/c, (0.4–1.5) GeV/c and (0.3–3) GeV/c, respectively. The fitting has been performed using χ^2 minimisation method keeping T_{kin}, β_s and n as free parameters. Here, n designates the order of the flow profile. The corresponding χ^2/ndf values for the fittings for each spherocity classes across all centralities are shown in Table 4.

Figure 9 shows the variation of kinetic freeze-out temperature (T_{kin}) versus mean transverse radial flow velocity ($\langle\beta_T\rangle$) for different spherocity and centrality classes obtained from simultaneous fit of identified charged particles' p_T spectra with BGBW function for Pb–Pb collisions at $\sqrt{s_{NN}}$ = 5.02 TeV. The shaded area shows the uncertainties from the simultaneous BGBW fits. As we move from central to peripheral collisions, T_{kin} increases and $\langle\beta_T\rangle$ decreases for all the spherocity classes. This behavior is naively expected due to the fact that central collisions are expected to have higher multiplicity in the final state, which would require more time to reach the freeze-out than the peripheral collisions. Conversely, with the increase in multiplicity one would expect higher

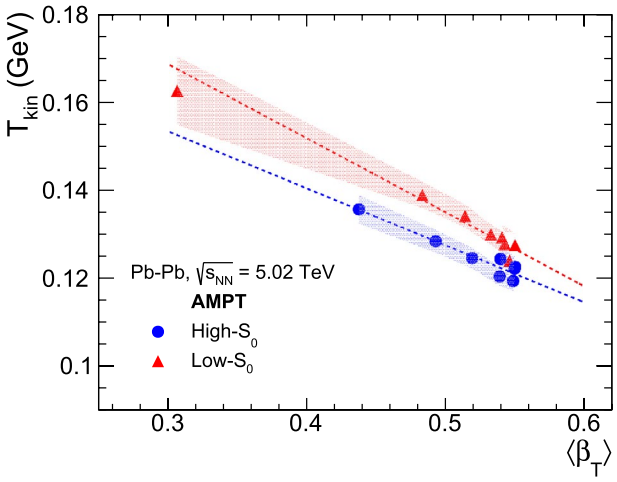

Figure 9. Kinetic freeze-out temperature versus mean transverse radial flow velocity obtained from simultaneous fit of identified particles' p_T-spectra with BGBW distribution function for high-S_0 (blue circle) and low-S_0 (red triangle) in Pb–Pb collisions at $\sqrt{s_{NN}}$ = 5.02 TeV. Linear fits for high-S_0 and low-S_0 are shown in dotted blue and red lines, respectively. The shaded area shows the uncertainties from the simultaneous BGBW fits.

	High-S_0		S_0 Integrated		Low-S_0	
Centrality(%)	$\langle\beta_T\rangle$	T_{kin} [GeV]	$\langle\beta_T\rangle$	T_{kin} [GeV]	$\langle\beta_T\rangle$	T_{kin} [GeV]
0–10	0.539 ± 0.007	0.124 ± 0.002	0.543 ± 0.006	0.123 ± 0.002	0.545 ± 0.007	0.124 ± 0.002
10–20	0.550 ± 0.007	0.123 ± 0.002	0.549 ± 0.006	0.123 ± 0.002	0.540 ± 0.008	0.129 ± 0.003
20–30	0.549 ± 0.006	0.122 ± 0.002	0.553 ± 0.006	0.122 ± 0.002	0.549 ± 0.007	0.128 ± 0.003
30–40	0.548 ± 0.007	0.120 ± 0.002	0.546 ± 0.006	0.123 ± 0.002	0.542 ± 0.007	0.128 ± 0.003
40–50	0.538 ± 0.006	0.121 ± 0.002	0.535 ± 0.006	0.125 ± 0.002	0.532 ± 0.007	0.130 ± 0.002
50–60	0.519 ± 0.007	0.125 ± 0.002	0.515 ± 0.007	0.129 ± 0.002	0.514 ± 0.008	0.134 ± 0.003
60–70	0.492 ± 0.008	0.129 ± 0.003	0.484 ± 0.008	0.134 ± 0.003	0.483 ± 0.009	0.139 ± 0.003
70–100	0.437 ± 0.010	0.136 ± 0.003	0.407 ± 0.015	0.145 ± 0.007	0.307 ± 0.021	0.163 ± 0.008

Table 5. Kinetic freeze-out temperature (T_{kin}) and mean transverse radial flow velocity ($\langle\beta_T\rangle$) obtained from simultaneous fit of identified charged particles' p_T-spectra with Boltzmann–Gibbs blastwave function.

transverse radial flow, which we observe in Fig. 9. The spherocity dependent values of $\langle\beta_T\rangle$ and T_{kin} for all centralities for Pb–Pb collisions at $\sqrt{s_{NN}}$ = 5.02 TeV are enlisted in Table 5.

Contrary to the observables studied so far in the previous sections, we see a clear dependence of the kinetic freeze-out parameters on S_0. An isotropic (high-S_0) event is expected to be dominated by large number of soft particles, which would require more time to reach the freeze-out. Thus, the isotropic events are found to have lower T_{kin} compared to low-S_0 events. To understand the dependence of the kinetic freeze-out parameters, we have fitted the parameters with a first-order polynomial function separately for each spherocity class. As evident from Fig. 9, the role of spherocity plays a bigger role in peripheral events and it diminishes when one goes towards central collisions. This could be an indication that spherocity is crucial while studying the final state effects.

Summary and conclusion

We have implemented transverse spherocity in Pb–Pb collisions at $\sqrt{s_{NN}}$ = 5.02 TeV using AMPT model and study the dependence of transverse spherocity on different global observables in heavy-ion collisions at the Large Hadron Collider energies. In summary, the spherocity distributions in Pb–Pb collisions are found to be shifted more towards the isotropic limit when compared to the pp collisions, where the distributions are shifted towards the jetty limit. This behavior is understood based on the fact that the system size in Pb–Pb collisions are significantly higher when compared with pp collisions and because of the medium effects through the process of isotropisation, the jettiness of the events gets suppressed to a larger extent. The Bjorken energy density and speed of sound are found to be independent of the spherocity selection in heavy-ion collisions. However, we found that kinetic freeze-out parameters depend on spherocity. The role of spherocity plays a bigger role in peripheral events and it diminishes when one goes towards central collisions. The sensitivity of event topology however, depends on the observable under study because of some of the counter-balancing effects in view of medium effects in heavy-ion collisions or high-multiplicity environments.

Received: 8 December 2021; Accepted: 15 February 2022
Published online: 10 March 2022

References

1. Mallick, N., Sahoo, R., Tripathy, S. & Ortiz, A. Study of transverse spherocity and Azimuthal anisotropy in Pb-Pb collisions at $\sqrt{s_{\rm NN}}$ = 5.02 TeV using A Multi-Phase Transport Model. *J. Phys. G* **48**, 045104. https://doi.org/10.1088/1361-6471/abeb59 (2021).
2. Lin, Z.-W., Ko, C. M., Li, B.-A., Zhang, B. & Pal, S. A Multi-phase transport model for relativistic heavy ion collisions. *Phys. Rev. C* **72**, 064901. https://doi.org/10.1103/PhysRevC.72.064901 (2005).
3. Wang, X.-N. & Gyulassy, M. HIJING: A Monte Carlo model for multiple jet production in p p, p A and A A collisions. *Phys. Rev. D* **44**, 3501. https://doi.org/10.1103/PhysRevD.44.3501 (1991).
4. Zhang, B. ZPC 1.0.1: A Parton cascade for ultrarelativistic heavy ion collisions. *Comput. Phys. Commun.* **109**, 193. https://doi.org/10.1016/S0010-4655(98)00010-1 (1998).
5. Greco, V., Ko, C. M. & Levai, P. Parton coalescence and anti-proton/pion anomaly at RHIC. *Phys. Rev. Lett.* **90**, 202302. https://doi.org/10.1103/PhysRevLett.90.202302 (2003).
6. Greco, V., Ko, C. M. & Levai, P. Parton coalescence at RHIC. *Phys. Rev. C* **68**, 034904. https://doi.org/10.1103/PhysRevC.68.034904 (2003).
7. Li, B., Sustich, A. T., Zhang, B. & Ko, C. M. Studies of superdense hadronic matter in a relativistic transport model. *Int. J. Mod. Phys. E* **10**, 267. https://doi.org/10.1142/S0218301301000575 (2001).
8. Li, B.-A. & Ko, C. M. Formation of superdense hadronic matter in high-energy heavy ion collisions. *Phys. Rev. C* **52**, 2037. https://doi.org/10.1103/PhysRevC.52.2037 (1995).
9. Fries, R. J., Müller, B., Nonaka, C. & Bass, S. A. Hadronization in heavy-ion collisions: Recombination and fragmentation of partons. *Phys. Rev. Lett.* **90**, 202303. https://doi.org/10.1103/PhysRevLett.90.202303 (2003).
10. Fries, R. J., Muller, B., Nonaka, C. & Bass, S. A. Hadron production in heavy ion collisions: Fragmentation and recombination from a dense parton phase. *Phys. Rev. C* **68**, 044902. https://doi.org/10.1103/PhysRevC.68.044902 (2003).
11. Tripathy, S., De, S., Younus, M. & Sahoo, R. Predictions for azimuthal anisotropy in Xe+Xe collisions at $\sqrt{s_{NN}} = 5.44$ TeV using a multiphase transport model. *Phys. Rev. C* **98**, 064904. https://doi.org/10.1103/PhysRevC.98.064904 (2018).
12. Loizides, C., Kamin, J. & d'Enterria, D. Improved Monte Carlo Glauber predictions at present and future nuclear colliders. *Phys. Rev. C* **97**, 054910. https://doi.org/10.1103/PhysRevC.97.054910 (2018). [Erratum: Phys. Rev. C 99, 019901 (2019)].
13. Cuautle, E. *et al.* Disentangling the soft and hard components of the pp collisions using the sphero(i)city approach (2014). arXiv:1404.2372 [hep-ph], .
14. Ortiz, A., Paić, G. & Cuautle, E. Mid-rapidity charged hadron transverse spherocity in pp collisions simulated with Pythia. *Nucl. Phys. A* **941**, 78. https://doi.org/10.1016/j.nuclphysa.2015.05.010 (2015).
15. Salam, G. P. Towards Jetography. *Eur. Phys. J. C* **67**, 637. https://doi.org/10.1140/epjc/s10052-010-1314-6 (2010).
16. Sjöstrand, T. *et al.* An introduction to PYTHIA 8.2. *Comput. Phys. Commun.* **191**, 159. https://doi.org/10.1016/j.cpc.2015.01.024 (2015).
17. Khuntia, A., Tripathy, S., Bisht, A. & Sahoo, R. Event shape engineering and multiplicity dependent study of identified particle production in proton + proton collisions at $\sqrt{s}$ = 13 TeV using PYTHIA8. *J. Phys. G* **48**, 035102. https://doi.org/10.1088/1361-6471/abb1f8 (2021).
18. Bjorken, J. D. Highly relativistic nucleus-nucleus collisions: The central rapidity region. *Phys. Rev. D* **27**, 140. https://doi.org/10.1103/PhysRevD.27.140 (1983).
19. Adam, J. *et al.* Measurement of transverse energy at midrapidity in Pb-Pb collisions at $\sqrt{s_{\rm NN}} = 2.76$ TeV. *Phys. Rev. C* **94**, 034903. https://doi.org/10.1103/PhysRevC.94.034903 (2016).
20. Sahoo, R., Mishra, A. N., Behera, N. K. & Nandi, B. K. Charged particle, photon multiplicity, and transverse energy production in high-energy heavy-ion collisions. *Adv. High Energy Phys.* **2015**, 612390. https://doi.org/10.1155/2015/612390 (2015). [Erratum: Adv. High Energy Phys. 2017, 4517153 (2017)].
21. Abelev, B. I. *et al.* Systematic measurements of identified particle spectra in pp, d^+ Au and Au+Au collisions from STAR. *Phys. Rev. C* **79**, 034909. https://doi.org/10.1103/PhysRevC.79.034909 (2009).
22. Karsch, F. Lattice results on QCD thermodynamics. *Nucl. Phys. A* **698**, 199. https://doi.org/10.1016/S0375-9474(01)01365-3 (2002).
23. Landau, L. D. On the multiparticle production in high-energy collisions. *Izv. Akad. Nauk Ser. Fiz.* **17**, 51 (1953).
24. Abbas, E. *et al.* Centrality dependence of the pseudorapidity density distribution for charged particles in Pb-Pb collisions at $\sqrt{s_{\rm NN}}$ = 2.76 TeV. *Phys. Lett. B* **726**, 610. https://doi.org/10.1016/j.physletb.2013.09.022 (2013).
25. Schnedermann, E., Sollfrank, J. & Heinz, U. W. Thermal phenomenology of hadrons from 200-A/GeV S+S collisions. *Phys. Rev. C* **48**, 2462. https://doi.org/10.1103/PhysRevC.48.2462 (1993).
26. Huovinen, P., Kolb, P. F., Heinz, U. W., Ruuskanen, P. V. & Voloshin, S. A. Radial and elliptic flow at RHIC: Further predictions. *Phys. Lett. B* **503**, 58. https://doi.org/10.1016/S0370-2693(01)00219-2 (2001).
27. Braun-Munzinger, P., Stachel, J., Wessels, J. P. & Xu, N. Thermal equilibration and expansion in nucleus-nucleus collisions at the AGS. *Phys. Lett. B* **344**, 43. https://doi.org/10.1016/0370-2693(94)01534-J (1995).
28. Tang, Z. *et al.* Statistical origin of constituent-quark scaling in the QGP hadronization. *Chin. Phys. Lett.* **30**, 031201. https://doi.org/10.1088/0256-307X/30/3/031201 (2013).
29. Adcox, K. *et al.* Single identified hadron spectra from s(NN)**(1/2) = 130-GeV Au+Au collisions. *Phys. Rev. C* **69**, 024904. https://doi.org/10.1103/PhysRevC.69.024904 (2004).

Acknowledgements

RS acknowledges the financial supports under the CERN Scientific Associateship and the financial grants under DAE-BRNS Project No. 58/14/29/2019-BRNS of Government of India. DB acknowledges the financial supports from CSIR, Government of India. SP acknowledges the financial supports from UGC, Government of India. ST acknowledges the supports under the INFN postdoctoral fellowship. The authors would like to acknowledge the usage of resources of the LHC grid computing facility at VECC, Kolkata and usage of resources of the LHC grid Tier-3 computing facility at IIT Indore. The authors acknowledge Dr. Arvind Khuntia and Mr. Dushmanta Sahu for careful reading of the manuscript.

Author contributions

All authors have equally contributed to the research article in terms of formulating the problem through discussions, data generation, data analysis, manuscript preparation, editing and correspondence.

Competing interests

The authors declare no competing interests.

Additional information

Correspondence and requests for materials should be addressed to R.S.

Reprints and permissions information is available at www.nature.com/reprints.

Publisher's note Springer Nature remains neutral with regard to jurisdictional claims in published maps and institutional affiliations.